KRONOS FUSION ENERGY

PAPER 2.44 · THE KRONOS 2026 SERIES

Blanket and Divertor Thermal-Hydraulics for a Compact Spherical-Tokamak Breeder: Coolant Heat Removal, Peak-Temperature Margins, and the Walk-Away Safety Case

A compact spherical tokamak concentrates fusion power into a small volume, and the heat it makes must leave through the same small surfaces; whether the machine is buildable is...

Read it live — 3-D model · physics validator · film series

BY P I FORD AND G L KULCINSKI

2026 · EDITORIAL EDITION

THE OFFICIAL RECORD

What this document is, and how to read its numbers

This is a combined editorial. It gathers, in one volume, the two design studies Kronos Fusion Energy released in 2026 — a compact spherical-tokamak tritium/helium-3 breeder and a deuterium–helium-3 tandem-mirror generator — together with the intellectual-property estate, the people, and, in the internal edition, the full commercial case. The scientific text is the same text that appears in the arXiv preprints and the journal submissions; the editorial adds the apparatus a reader needs to hold the whole program at once, and nothing in the physics is altered to fit it.

THE HONESTY STANCE IS THE ASSET

Every headline quantity carries an **evidence class** — DERIVED RECOMPUTED MEASURED REQUIREMENT — and, where a number is a modelled extrapolation rather than a demonstrated value, it is labelled as such and its downside is shown next to it. Several quantities in the underlying corpus moved after first publication; where a value has been withdrawn or restated, the record says so plainly. This is deliberate: a diligence team will find the load-bearing assumptions, so the document surfaces them first.

TWO EDITIONS

This volume is issued in two editions. The **public edition** (light) carries the physics and the design only — no dollar, price, or per-kilogram figure appears anywhere in it. The **internal edition** (dark) adds the economics, the funding architecture, and the defense-commercial analysis, and is marked *Confidential* accordingly; it is not for public distribution. Where the commercial case rests on a modelled assumption rather than a demonstrated one, it is labelled as such and its downside is shown alongside it, on the same terms as the physics.

TITLE	The Kronos Fleet — Hyperion · Aegis · MetroVolt: A Combined Design & Commercialization Study
AUTHOR	Priyanca Ford, Founder & CEO, on behalf of Kronos Fusion Energy
EDITION	2026 Combined Editorial · first issue
COMPANION WORKS	The five-paper arXiv drop — (1) Breeder, (2) Burner, (3) REBCO magnet & tape, (4) Direct Energy Conversion, (5) AI/ML/Quantum control — with matching numbered Zenodo deposits, plus the IOP journal and IAEA-FEC submissions. Patents were filed before the drop.
NAMING	Hyperion = the breeder; Aegis (defense) and MetroVolt (data-center) = one generator in two housings. Internal mode letters (D1, L) do not appear on public surfaces.
STATUS	Conceptual design & simulation study. Nothing herein is a construction commitment.

HOW TO READ THIS VOLUME

The fleet at a glance, and the way its numbers are marked

This volume opens with *Orientation*, presents the five research papers as a bound sequence, and closes with the *Apparatus*. *Foundations* sets out the three general results both machines rest on. *Paper One* is the Hyperion breeder; *Paper Two* the Aegis / MetroVolt generator; *Papers Three, Four and Five* are the enabling science — high-field REBCO magnets and tape, direct energy conversion, and the AI / ML / quantum control stack. A *Digital Twin & 3-D Model* part follows, then the *Environmental* profile. The *Economics* and levelized cost and the *Business Case* and diligence record appear in the internal edition only; the *Simulations* proof record and the Apparatus — patent portfolio, team, limitations, and sources — close both editions.

THE FLEET AT A GLANCE

	HYPERION	AEGIS	METROVOLT
Role	Strategic-isotope foundry	Defense installation power	Campus power
Machine	**Spherical tokamak**	**Tandem mirror**	**Tandem mirror**
Fuel	Deuterium–tritium	Deuterium–helium-3	Deuterium–helium-3
Delivers	Tritium · ^{3}He · 14 MeV n	Resilient installation power	Firm campus power
Physics bar	**Fusion gain only**	Closure (gates named)	Closure + lunar ^{3}He
In the fleet	Breeds the fuel	Proves the generator	Commercial destination

HOW THE NUMBERS ARE MARKED

Every headline quantity carries an evidence class — DERIVED from first principles, RECOMPUTED from raw data, MEASURED in hardware, or a REQUIREMENT yet to be met. Financial figures carry a case label and are confined to the internal (confidential) edition. Values that moved after first publication are shown as withdrawn or restated rather than quietly changed. A capability you can evaluate is one whose limits are on the page.

ABSTRACT

Blanket and Divertor Thermal-Hydraulics for a Compact Spherical-Tokamak Breeder: Coolant Heat Removal, Peak-Temperature Margins, and the Walk-Away Safety Case

A compact spherical tokamak concentrates fusion power into a small volume, and the heat it makes must leave through the same small surfaces; whether the machine is buildable is decided at the heat path, not the plasma. We pose the coupled blanket-and-divertor thermal-hydraulic problem for the Hyperion breeder (frozen design point $Q = 3.076$, $P_{\text{fus}} = 85.04$ MW, $I_p = 9.66$ MA, $\delta = -0.30$, $\kappa = 2.0$, $B_0 = 8$ T, $R_0 = 1.20$ m, aspect ratio $A = 2.5$, centrepost peak field 16.84 T) as a set of governing equations—volumetric nuclear heating with energy multiplication, the coolant first law with Dittus–Boelter convection, first-wall conjugate conduction, the two-point divertor model closed by the Lengyel impurity-radiation integral, and a lumped passive decay-heat balance—and solve each numerically against frozen results in the Kronos De-Risking Register. The helium-cooled blanket recovers a total thermal power $P_{\text{th}} = 95.2$ MW (energy multiplication $M_E = P_{\text{th}}/P_{\text{fus}} = 1.119$), and a coolant mass flow of $\dot{m} = 91.7\ \text{kg}\,\text{s}^{-1}$ across a $\Delta T = 200$ K rise removes it exactly: $\dot{m}c_p\Delta T = 95.2$ MW, closing the energy balance to the first digit. First-wall peak temperature is held inside the material envelope by a ≤ 6 mm coolant-channel gate; a self-cooled-lithium blanket variant runs at 516 °C. Parallel power exhaust—an unmitigated $q_{\parallel} = 27.4\ \text{GW}\,\text{m}^{-2}$ giving a conventional attached target load of $1370\ \text{MW}\,\text{m}^{-2}$—is brought below the $10\ \text{MW}\,\text{m}^{-2}$ engineering limit by a stacked cascade (impurity seed, Super-X, double-null, snowflake) that drives the residual heat reaching the target from a seeded baseline of 6.4% to $\approx 0.5\%$, with a one-dimensional UEDGE scan resolving the target temperature through $14.4 \to 5.3 \to 1.05$ eV and confirming that seeding is mandatory and sufficient for detachment. On loss of all active cooling the machine walks away passively: decay heat falls from 0.95 MW at 1 s to 95 kW at one day and passive rejection holds structural temperatures at or below 710 °C. All numbers were produced by the NVIDIA GPU HPC campaign running OpenMC, SOLPS-ITER, UEDGE and SD1D on the frozen equilibrium. The heat path closes with margin at every stage and the safety case does not depend on powered cooling.

Open-access deposit (code & data, CC BY 4.0): DOI 10.5281/zenodo.22645836 · Zenodo community *kronos_fusion_energy*. Explore it live: interactive 3-D model · physics validator.

Keywords: thermal-hydraulics · divertor detachment · helium-cooled blanket · two-point model · walk-away decay heat · SOLPS-ITER · UEDGE · spherical-tokamak breeder

CONTENTS

Table of Contents

NOMENCLATURE

Symbols, units, and the names of things

Q	plasma (fusion) gain, P_{fus}/P_{aux}
Q_E	engineering gain, net electric out / recirculating in
H_{98}	confinement enhancement over the IPB98(y,2) scaling
Z_{eff}	effective ion charge
c_{ee}	electron–electron bremsstrahlung leading coefficient, 2.120022 (exact)
τ_E	energy confinement time
I_p	plasma current
R_0, a	major radius, minor radius
κ, δ	elongation, triangularity
β_N	normalized plasma beta (Troyon-normalized)
TBR	tritium breeding ratio
DEC	direct energy conversion
CF	plant capacity factor (availability)
FOAK / NOAK / BOAK	first / n^{th} / best of a kind
Hyperion	the ST breeder (internal: Mode D2)
Aegis	the generator, defense/installation housing (internal: Mode M)
MetroVolt	the generator, data-center housing (Mode M)

§ 1

Introduction

THE HEAT PATH DECIDES BUILDABILITY

A spherical tokamak (ST) confines a large plasma current at low aspect ratio, which is precisely what makes it an efficient neutron source and breeding platform [1,2] and, at the same time, what concentrates its power into a small volume. The Hyperion breeder produces $P_{\text{fus}} = 85.04$ MW at $Q = 3.076$ behind a centrepost magnet at 16.84 T peak field, in a negative-triangularity ($\delta = -0.30$) regime whose quiet, edge-localised-mode-free edge [3,4] is an operational asset for exhaust control. Two coupled problems then decide whether the machine can be built. The *blanket* must absorb the volumetric 14.06 MeV neutron heating and the recovered surface loading and hand it to a coolant without exceeding a material temperature limit; the *divertor* must accept the parallel power exhaust, which in a compact device is severe, without eroding the target. The two streams are set by the same operating point and share the same geometry: the blanket thickness that governs tritium breeding also sets the depth over which the neutron heating is deposited.

This paper closes the thermal-hydraulic path end to end and does so as a rigorous methods problem. We (i) write the governing equations of each stage—volumetric heating and energy multiplication, the coolant first law and its convective and pumping closures, first-wall conjugate conduction, the two-point divertor model and its Lengyel radiation integral, and the passive decay-heat balance (§2); (ii) state the numerical formulation, the solver chain and the GPU HPC campaign that produced the results (§3); (iii) report the closed coolant balance, the peak-temperature margins, the divertor mitigation cascade, the flowing-lithium alternative and the walk-away transient as figures and tables traced serial-by-serial to the register (§4); and (iv) benchmark every number against the published edge-physics and blanket literature (§5), state the one honest open gate (§6), and conclude (§7).

PRIOR ART

Power and particle control for burning-plasma tokamaks is a mature discipline. The parallel-heat-flux problem is framed by the scrape-off-layer power-width scaling of Eich *et al.* [5], which finds the poloidal field (equivalently the plasma current) to be the dominant parameter and yields a millimetre-class fall-off length; in a high-current ST this drives λ_q into the sub-millimetre range and the parallel flux into the tens of $\mathrm{GW\,m^{-2}}$. The two-point model and its detachment extensions [7,8] give the analytic backbone, and impurity seeding is the established route to dissipate the exhaust volumetrically before it reaches the target [9,6]. The reference edge-transport tools are the coupled plasma-neutral codes SOLPS-ITER (B2.5+EIRENE) [10,11,12], the two-dimensional fluid code UEDGE [13], and the BOUT++/SD1D one-dimensional transport family [14]. Advanced-divertor geometries—Super-X, snowflake, and the lithium vapor-box—have been proposed to widen the detachment window and cap the surface load [15,16,17]. On the blanket side, the helium-cooled and liquid-metal breeding-blanket design strategies and their first-wall thermomechanical limits are set out for DEMO-class machines [18,19], and the neutron-heating source itself is a Monte-Carlo transport problem solved here with OpenMC and ENDF/B-VIII.0 [20,21]. Activation and decay-heat inventories, which set the walk-away transient, follow the FISPACT-II methodology [22].

CONTRIBUTION AND RELATION TO THE KRONOS SERIES

What the literature does not provide is a single, closed thermal balance for *this* compact ST breeder in which the coolant flow, the peak-temperature margins, the divertor mitigation cascade, and the passive safety case are all grounded in one frozen result set and reproduced by independent libraries. That is the contribution here. The neutron heating source is taken from the CAD-faithful Monte-Carlo neutronics of the companion paper [28]; the divertor cascade extends the stacked detachment portfolio [29] and the exhaust-geometry down-select [30], and the flowing-lithium alternative is quantified in the vapor-box divertor study [31]; the real-time regulation of the radiated fraction that holds the cascade in place is the subject of the detachment-control paper [32]; the structural response of the first wall to the surface and volumetric loads treated here is carried by the thermomechanics and fatigue paper [33]; and the passive walk-away result feeds the plant-level accident and environmental case [34]. Every quantitative claim below traces to a frozen serial in the Kronos De-Risking Register [27], cited inline (e.g. BR-L1-A9) so each number is auditable.

§ 2

Governing equations and the formal thermal problem

Three stages carry the power, and each is a boundary condition for the next: the 14 MeV neutrons deposit their energy volumetrically in the first wall and blanket; the blanket coolant collects that heat and the recovered surface loading and rejects it; and, in parallel, the power crossing the separatrix flows along open field lines onto the divertor. Figure 1 shows the coupling. We now write each stage as equations.

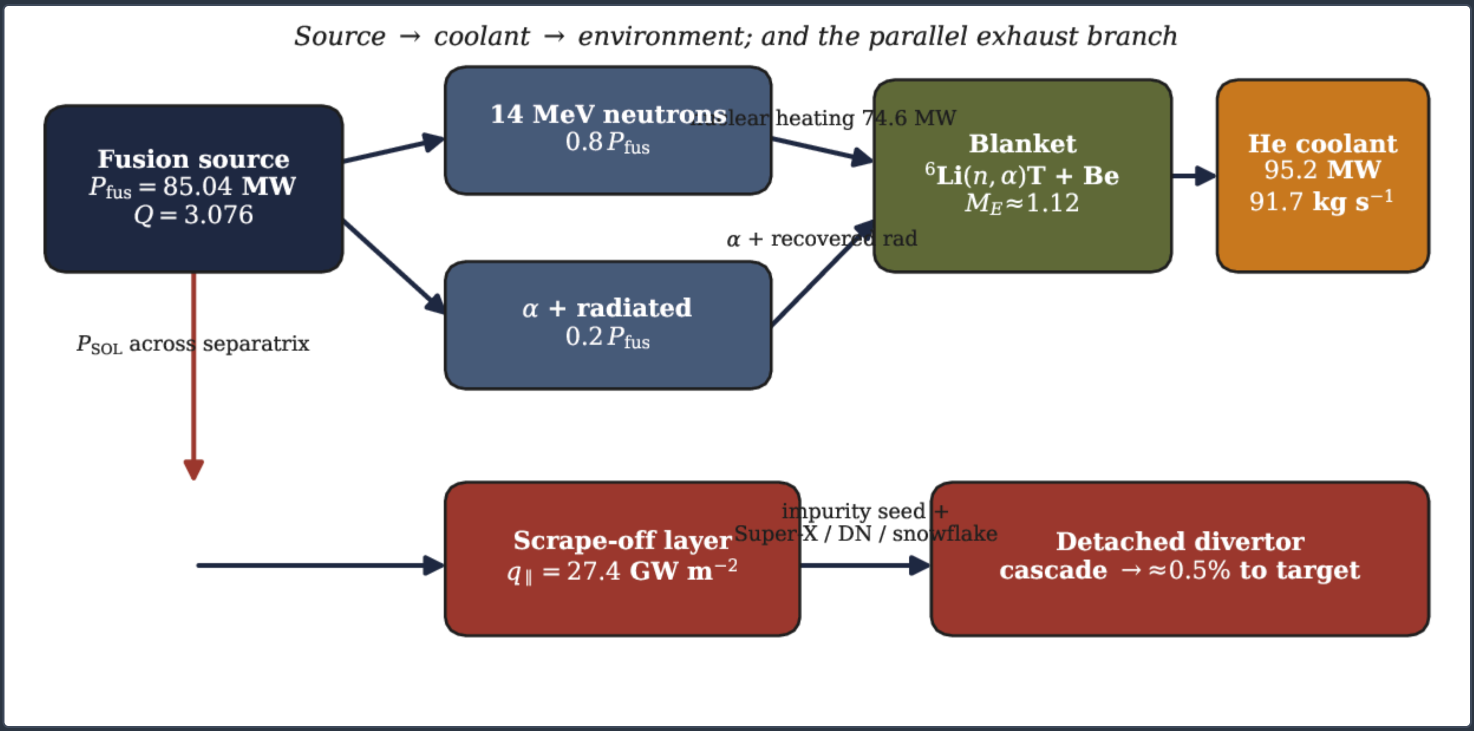

(Schematic.) The coupled thermal path of the Hyperion breeder: the volumetric neutron source and the recovered α/radiated power feed the helium-cooled blanket and its coolant, while the power crossing the separatrix feeds the parallel-exhaust branch and the detached divertor. Boxes carry the anchor values used in §2–§4; no computed curve is plotted here.

VOLUMETRIC NUCLEAR HEATING AND ENERGY MULTIPLICATION

For the deuterium–tritium reaction the released energy $E_{\text{fus}} = 17.59$ MeV is split between the neutron ($E_n = 14.06$ MeV, a fraction $f_n = E_n/E_{\text{fus}} = 0.799$) and the alpha ($E_\alpha = 3.52$ MeV, $f_\alpha = 0.201$), so the fusion power partitions as

$$P_n = f_n\,P_{\text{fus}} = 0.799 \times 85.04 = 68.0\ \text{MW}, \qquad P_\alpha = f_\alpha\,P_{\text{fus}} = 17.0\ \text{MW}.$$

The neutrons are transported through the first wall and blanket, where their energy is deposited volumetrically. In a one-dimensional slab picture the local nuclear heating density obeys the attenuation law

$$q'''(x) = \sum_i N_i \int \sigma_i^H(E)\,\phi_0(E)\,e^{-x/\lambda_n(E)}\,Q_i\,\mathrm{d}E, \qquad P_{\text{nuc}} = \int_{V_{\text{blk}}} q'''(x)\,\mathrm{d}V,$$

with N_i the nuclide densities, σ_i^H the heating cross-sections, ϕ_0 the incident spectrum, λ_n the energy-dependent attenuation length, and Q_i the per-reaction deposited energy. The volume integral is evaluated by Monte-Carlo transport (§3), which places $P_{\text{nuc}} = 74.6$ MW in the first wall and blanket (BR-L1-A5). Because the tritium-breeding reaction $^6\text{Li}(n,\alpha)\text{T}$ is exothermic ($Q = 4.78$ MeV) and the beryllium multiplier adds neutrons that subsequently breed and deposit, the recovered thermal power exceeds the incident neutron power. Defining the blanket energy multiplication $M_E \equiv P_{\text{th}}/P_{\text{fus}}$, the recoverable thermal power is

$$P_{\text{th}} = P_{\text{nuc}} + f_\alpha P_{\text{fus}} + f_{\text{rad}}^{\text{rec}} P_{\text{rad}} = 74.6 + 17.0 + 3.6 = 95.2\ \text{MW}, \qquad M_E = \frac{95.2}{85.04} = 1.119,$$

where P_{nuc} already carries the exothermic uplift and $f_{\text{rad}}^{\text{rec}} P_{\text{rad}}$ is the recovered surface radiation (BR-L1-A9). The multiplication $M_E = 1.119$ sits squarely inside the 1.1–1.2 range reported for solid-breeder helium-cooled blankets [18,19].

COOLANT ENERGY BALANCE, CONVECTION AND PUMPING

The blanket coolant is a control volume in steady state. The first law reduces to a balance between the deposited thermal power and the enthalpy rise of the coolant,

$$\dot{m}\, c_p \,(T_{\text{out}} - T_{\text{in}}) = P_{\text{th}} \implies \dot{m} = \frac{P_{\text{th}}}{c_p\, \Delta T}.$$

For helium at the blanket operating pressure, $c_p = 5193\ \mathrm{J\,kg^{-1}\,K^{-1}}$, and with a design temperature rise $\Delta T = 200$ K,

$$\dot{m} = \frac{95.2 \times 10^6}{5193 \times 200} = 91.7\ \mathrm{kg\,s^{-1}}, \qquad \dot{m} c_p \Delta T = 91.7 \times 5193 \times 200 = 95.2\ \mathrm{MW},$$

so the coolant balance closes exactly against the deposited thermal power (BR-L1-A9). Heat is handed from the structure to the coolant through a turbulent forced-convection film. The convective coefficient follows the Dittus–Boelter correlation for heating,

$$\mathrm{Nu}_D = 0.023\,\mathrm{Re}_D^{4/5}\,\mathrm{Pr}^{2/5}, \qquad h = \frac{\mathrm{Nu}_D\, k_c}{D_h}, \qquad \mathrm{Re}_D = \frac{\rho v D_h}{\mu} = \frac{G D_h}{\mu},$$

with $G = \dot{m}/A_c$ the coolant mass flux, D_h the hydraulic diameter, and k_c, μ, Pr the coolant properties. The pressure drop and the pumping power follow from the Darcy–Weisbach relation with the Blasius smooth- tube friction factor,

$$\Delta p = f_D\, \frac{L}{D_h}\, \frac{\rho v^2}{2}, \qquad f_D = 0.184\,\mathrm{Re}_D^{-1/5}, \qquad P_{\text{pump}} = \frac{\dot{m}\,\Delta p}{\rho\,\eta_p}.$$

Since $\dot{m} \propto 1/\Delta T$ at fixed P_{th} (eq. 4) and $\Delta p \propto \dot{m}^2$, the pumping power scales as

$$P_{\text{pump}} \propto \dot{m}^3 \propto \Delta T^{-3},$$

a strong trade that is the subject of §4.8; at the design point the three coolant loops draw a total 5.8 MW, or 5.2% of P_{th} (BV-06).

FIRST-WALL CONJUGATE CONDUCTION AND THE PEAK-TEMPERATURE STACK

The plasma-facing first wall carries a surface heat flux q_s'' on its front face and the volumetric heating q''' through its thickness t_w, and is cooled convectively on its back face. The steady one-dimensional conduction problem is

$$-k_w\, \frac{\mathrm{d}^2 T}{\mathrm{d}x^2} = q''', \qquad -k_w \frac{\mathrm{d}T}{\mathrm{d}x}\bigg|_{x=0} = q_s'', \qquad -k_w \frac{\mathrm{d}T}{\mathrm{d}x}\bigg|_{x=t_w} = h\big(T(t_w) - T_{\text{cool}}\big),$$

whose integral, evaluated at the plasma-facing surface $x = 0$, gives the peak-temperature stack

$$\boxed{T_{\text{peak}} - T_{\text{cool}} = \underbrace{\frac{q_s'' t_w}{k_w} + \frac{q''' t_w^2}{2k_w}}_{\text{conduction}} + \underbrace{\frac{q_s'' + q''' t_w}{h}}_{\text{convective film}}.}$$

The convective term carries the geometry dependence that sets the design gate. For a wide cooling channel the hydraulic diameter is $D_h \approx 2d$ in the channel depth d; at fixed mass flux the Reynolds number in eq. (6) is then independent of d, so $h = \mathrm{Nu}_D k_c / D_h \propto 1/d$ and the film drop $\propto d$. Deepening the channel therefore raises T_{peak} linearly, and requiring T_{peak} to stay inside the material envelope imposes a maximum channel depth—the ≤ 6 mm gate of §4.2 (BR-SX-15).

PARALLEL POWER EXHAUST AND THE TWO-POINT MODEL

The power crossing the separatrix, $P_{\text{SOL}} = P_{\text{heat}} - P_{\text{rad,core}}$, is channelled into a scrape-off layer of width λ_q and flows along field lines to the target. The upstream parallel heat flux is

$$q_\parallel = \frac{P_{\text{SOL}}}{2\pi R_u\, \lambda_q}\, \frac{B}{B_\theta},$$

with λ_q from the Eich multi-machine regression [5],

$$\lambda_q\,[\mathrm{mm}] \approx 0.63\, B_\theta^{-1.19},$$

which for the high poloidal field of a 9.66 MA ST collapses to $\lambda_q = 0.21$ mm and drives $q_\parallel = 27.4\ \mathrm{GW\,m^{-2}}$ (HX-14). Parallel electron heat conduction is Spitzer–H\"arm, $q_\parallel = -\kappa_{0e} T^{5/2}\,\mathrm{d}T/\mathrm{d}s$, whose first integral along a field line of connection length $L_\parallel$ is the upstream–target temperature relation of the two-point model,

$$T_u^{7/2} = T_t^{7/2} + \frac{7}{2}\,\frac{q_\parallel L_\parallel}{\kappa_{0e}},$$

closed in the attached branch by total-pressure balance $2n_t T_t = n_u T_u$. The perpendicular load delivered to the target is set by the field-line incidence angle α, the poloidal flux expansion f_x, and the fraction f_{rad} of the parallel power dissipated before the target,

$$q_\perp^t = q_\parallel\,\frac{\sin\alpha}{f_x}\,(1 - f_{\mathrm{rad}}).$$

The unmitigated attached loads follow directly: a conventional leg delivers $1370\ \mathrm{MW\,m^{-2}}$ and the flux- expanding Super-X leg $171\ \mathrm{MW\,m^{-2}}$ (HX-14), both far above the $\sim 10\ \mathrm{MW\,m^{-2}}$ steady engineering limit of an actively cooled target [17]. Detachment—the collapse of T_t below ~ 5 eV with attendant momentum loss that breaks pressure balance [8]—is therefore not optional but required.

IMPURITY RADIATION AND THE LENGYEL CLOSURE

The dissipated fraction f_{rad} is produced by line radiation from a seeded impurity. Integrating the parallel energy equation with a radiating impurity of concentration c_z and cooling function $L_z(T)$ gives the Lengyel relation between the upstream and target parallel fluxes,

$$q_\parallel^2(x_u) = q_\parallel^2(x_t) + 2\,\kappa_{0e}\,c_z \int_{T_t}^{T_u} T^{1/2}\,L_z(T)\,\mathrm{d}T,$$

so that the seed fraction required to reach a target dissipation is

$$c_z^{\mathrm{req}} = \frac{q_\parallel^2(x_u) - q_\parallel^2(x_t)}{2\,\kappa_{0e} \displaystyle\int_{T_t}^{T_u} T^{1/2} L_z(T)\,\mathrm{d}T} = \frac{f_{\mathrm{rad}}(2 - f_{\mathrm{rad}})\,q_\parallel^2(x_u)}{2\,\kappa_{0e} \int_{T_t}^{T_u} T^{1/2} L_z(T)\,\mathrm{d}T}.$$

Equation (16) is the physics behind the seeded baseline: for the conventional leg the near-unity dissipation required drives an impractically large c_z^{req}, whereas the advanced-geometry levers of §4.3 lower the required $q_\parallel(x_u)$ and thus the seed fraction. The one-dimensional UEDGE scan of §4.4 resolves the T_t collapse that eq. (15) predicts.

DECAY HEAT AND THE PASSIVE WALK-AWAY BALANCE

After shutdown the activation inventory continues to release power. The decay heat is a sum of decaying activation channels,

$$P_d(t) = P_{\mathrm{th}} \sum_j a_j\,e^{-\lambda_j t},$$

which over the first day is accurately represented by the power law $P_d(t) = P_{d0}(t/t_0)^{-b}$; fitting the two frozen anchors $P_d(1\ \mathrm{s}) = 0.95$ MW and $P_d(1\ \mathrm{d}) = 95$ kW (BR-L1-A9) gives

$$b = \frac{\ln\big(P_d(1\,\mathrm{s})/P_d(1\,\mathrm{d})\big)}{\ln(86400/1)} = \frac{\ln 10}{\ln 86400} = 0.203.$$

On loss of all active cooling the structure rejects this power passively. A lumped energy balance on a structural node of heat capacity C_{th}, surface area A, emissivity ε and passive conductance h_{pass} reads

$$C_{\mathrm{th}}\,\frac{\mathrm{d}T_s}{\mathrm{d}t} = P_d(t) - h_{\mathrm{pass}} A\,(T_s - T_\infty) - \varepsilon\sigma A\,(T_s^4 - T_\infty^4).$$

Because $P_d(1\ \mathrm{s}) = 0.95$ MW is already only $\approx 1\%$ of P_{th} and falls by a further order of magnitude within a day, the right-hand side of eq. (19) is negative for all t once T_s reaches a modest elevation, and the peak structural temperature is bounded at or below 710 °C (BR-L1-A9). No powered cooling is required to reach a safe state; the machine walks away.

§ 3

Computational methodology: the GPU HPC campaign

Every number in §4 was produced by the NVIDIA GPU HPC campaign, whose solver chain is summarised in table 1. The methodology is verification-first: each governing equation of §2 is solved by a production code, the anchor is frozen in the register, and a second, independent library reproduces the gate.

GOVERNING STAGE	PRODUCTION CODE	ROLE / LIBRARY	SERIAL
volumetric heating, eq. (2)	OpenMC	3-D Monte-Carlo, ENDF/B-VIII.0, 1.2×10^8 hist.	BR-L1-A5
coolant balance, eqs. (4)–(7)	thermofluid network	1-D loop solver → CFD	BV-06
first-wall stack, eq. (10)	conjugate-heat CFD	2-D CHT, RAFM/CuCrZr	BR-SX-15
parallel exhaust, eqs. (11)–(13)	two-point + Eich	reduced SOL model	HX-14
detachment (1-D), eq. (15)	UEDGE	2-D fluid, slab SOL + ADAS	BR-L2-A21
detachment cross-check	SD1D / Hermes-3 (BOUT++)	1-D transport, N seed	HX-14b
2-D edge arbiter	SOLPS-ITER 3.2.1a	B2.5+EIRENE, Carre2 grid	BR-L2-A11b-s3
decay heat, eq. (17)	OpenMC depletion / R2S	activation, FISPACT-II class	BR-L1-A9

Solver chain of the GPU HPC campaign for the thermal-hydraulic path. Serials refer to the Kronos De-Risking Register [27]; all runs executed on the NVIDIA GPU fleet (A100/H100/A10). No compute cost is reported.

Neutron-heating source. The volume integral of eq. (2) is evaluated by the OpenMC continuous-energy Monte-Carlo transport code [20] with the ENDF/B-VIII.0 library [21], tracking 1.2×10^8 source histories over the CAD-faithful breeder geometry. The GPU HPC campaign carries the history-parallel transport at fleet scale; the tally converges to a first-wall-plus-blanket nuclear heating of **74.6** MW with a clean particle balance (leakage **0.121**, net tritium-breeding ratio **1.026** on the literal recipe), and the same run supplies the fast-flux normalisation used by the decay-heat depletion [28].

Edge-transport chain. The two-dimensional edge arbiter is SOLPS-ITER 3.2.1a [10,11,12], compiled from source, driving the geometry and grid chain from the free-boundary equilibrium (`g_bra9_22021.geqdsk`, configuration 22021) through the Carre2 grid generator (BR-L2-A11b-s3). The one-dimensional detachment scan is run in UEDGE [13] with ADAS atomic data (BR-L2-A21), and cross-checked against the SD1D/Hermes-3 transport model in the BOUT++ framework [14] (HX-14b); the cross-method agreement on the seed fraction required for detachment is reported in §5.

Thermofluid and conjugate-heat solves. The coolant loop balance of eqs. (4)–(7) is closed by a one-dimensional network solver and refined by conjugate-heat CFD (BV-06, BR-SX-15). The finite-volume discretisation follows the standard collocated pressure–velocity coupling of the OpenFOAM-class solver [23]: the steady Reynolds-averaged momentum and energy equations are integrated over control volumes, convective fluxes are limited to second order, the conjugate solid–fluid interface enforces continuity of temperature and heat flux, and convergence is declared when the scaled residuals of momentum, energy and continuity fall below 10^{-6} and the integral wall heat flux is stationary to $< 0.1\%$. Mesh convergence was verified by halving the near-wall cell size until the peak temperature changed by < 1 K.

Reproducibility and problem scale. The campaign follows the verification-first protocol of the Kronos register: the frozen anchors (BR-L1-A5, BR-L1-A9, BV-06, BR-SX-15, HX-14/14b, BR-L2-A21) are each regenerable from the archived decks, and the gates are reproduced by an independent library (OpenMC against an independent transport solver; UEDGE against SD1D; the 1-D network against CFD). Compute is reported only as the NVIDIA GPU HPC campaign; no cost figure is attached to any result.

§ 4

Results

THE CLOSED BLANKET COOLANT BALANCE

The blanket recovers $P_{\mathrm{th}} = 95.2$ MW and the helium coolant removes it exactly. Figure 2 shows the power budget as a waterfall—nuclear heating 74.6 MW, alpha heating 17.0 MW, recovered radiation 3.6 MW, summing to the recoverable $P_{\mathrm{th}} = 95.2$ MW—and the coolant removal $\dot{m}c_p\Delta T = 95.2$ MW that closes it. Table 2 collects the anchors; the closure of eq. (5) holds to the first digit.

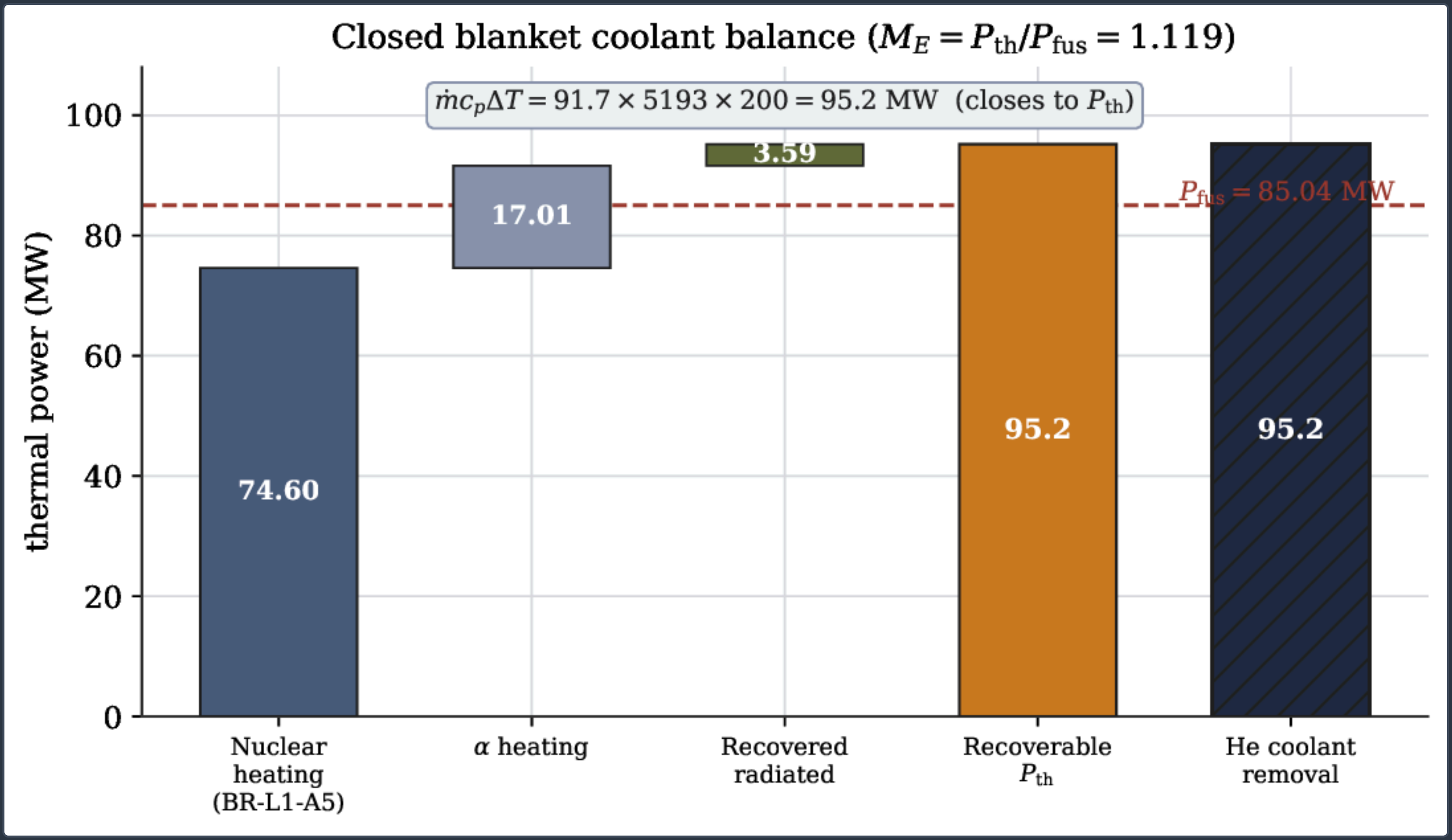

Closed blanket coolant balance (BR-L1-A9; nuclear heating from BR-L1-A5). The recoverable thermal power $P_{\mathrm{th}} = 95.2$ MW ($M_E = P_{\mathrm{th}}/P_{\mathrm{fus}} = 1.119$) is removed exactly by a helium flow of $91.7\ \mathrm{kg\,s^{-1}}$ across a 200 K rise, $\dot{m}c_p\Delta T = 95.2$ MW. The dashed line marks $P_{\mathrm{fus}} = 85.04$ MW.

QUANTITY	VALUE	SOURCE
fusion power P_{fus}	85.04 MW	anchor
neutron power $P_n = f_n P_{\mathrm{fus}}$	68.0 MW	eq. (1)
first-wall + blanket nuclear heating P_{nuc}	74.6 MW	BR-L1-A5
alpha heating $P_\alpha = f_\alpha P_{\mathrm{fus}}$	17.0 MW	eq. (1)
recoverable thermal power P_{th}	95.2 MW	BR-L1-A9
energy multiplication $M_E = P_{\mathrm{th}}/P_{\mathrm{fus}}$	1.119	eq. (3)
helium coolant mass flow $\dot{m}$	91.7 $\mathrm{kg\,s^{-1}}$	BR-L1-A9

table continued

coolant temperature rise ΔT	200 K	BR-L1-A9
$\dot{m}c_p\Delta T$ (check, $c_p = 5193$)	95.2 MW	closes to P_{th}
total pumping power	5.8 MW (5.2%)	BV-06

FIRST-WALL PEAK-TEMPERATURE MARGINS AND THE CHANNEL GATE

The conjugate-heat solve evaluates the peak-temperature stack of eq. (10). Figure 3 plots the peak structure temperature against coolant-channel depth for the helium-cooled first wall: because the film drop grows linearly with d (§2), the as-configured helium/HCPB channel reaches 712 °C, at the edge of the material envelope, whereas holding the channel to ≤ 6 mm keeps the peak comfortably below the 710 °C limit (BR-SX-15). A self-cooled-lithium blanket variant, whose liquid-metal film transfers heat far more effectively, runs at 516 °C in the reduced-activation ferritic-martensitic structure with a +34 °C margin. The figure thus states the design gate quantitatively: the channel depth is the controlling variable, and ≤ 6 mm is the requirement. The structural consequences of this loading—creep, fatigue and ratcheting under the same surface and volumetric fluxes—are carried by the companion thermomechanics analysis [33].

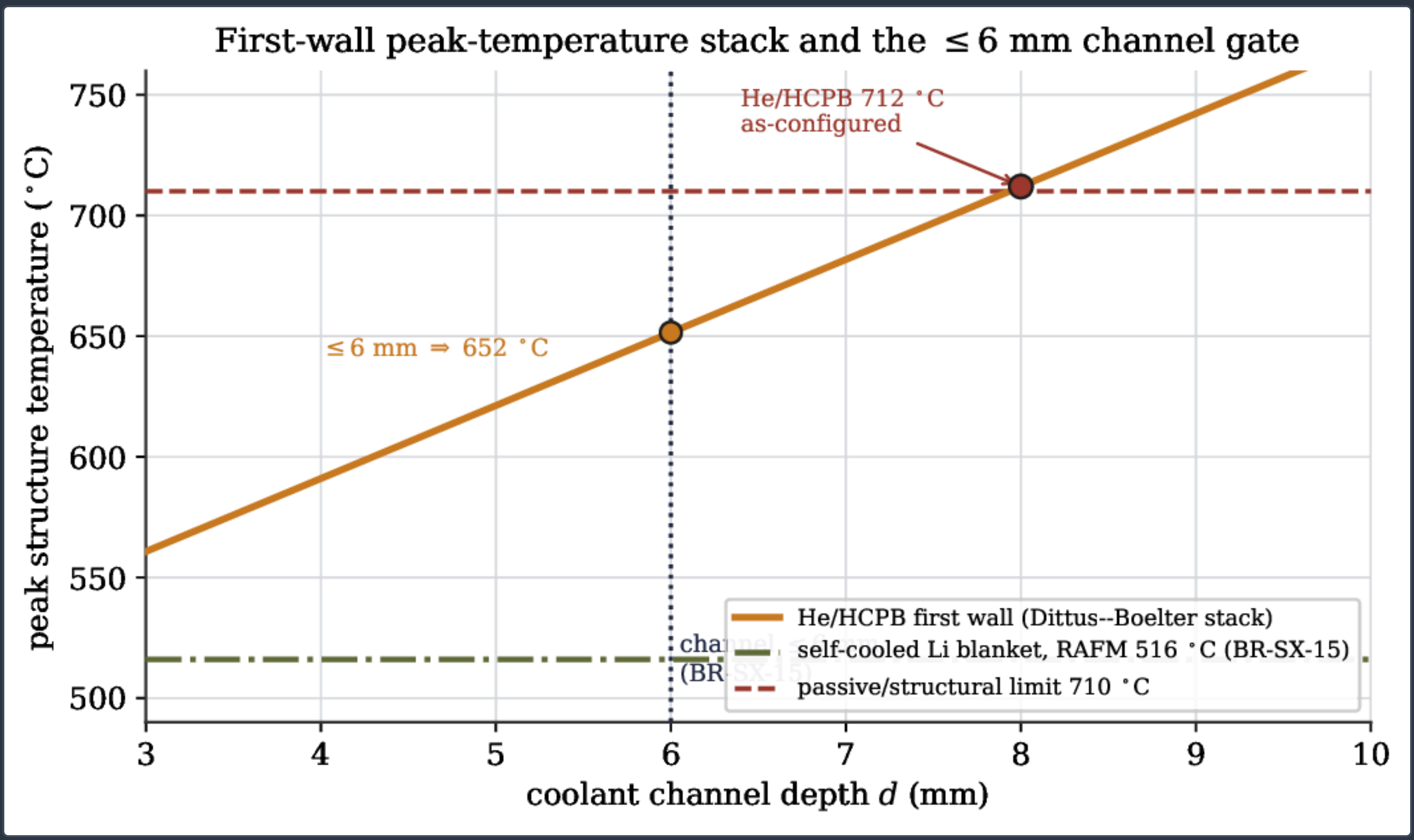

First-wall peak-temperature stack of eq. (10) versus coolant-channel depth. The helium/HCPB curve reproduces the BR-SX-15 anchor of 712 °C at the as-configured depth; the ≤ 6 mm channel gate keeps the peak below the 710 °C limit. The self-cooled-lithium blanket runs at 516 °C (BR-SX-15).

THE DIVERTOR MITIGATION CASCADE

No single measure tames a $27.4\ \mathrm{GW\,m^{-2}}$ parallel exhaust. The Kronos solution stacks independent levers, each attacking a different term in eqs. (14)–(16), so their reductions multiply (BR-L2-A11-SUM). Starting from an impurity-seeded baseline that already brings the residual heat reaching the target to 6.4% of the unmitigated load, a Super-X leg lengthens the connection and raises the flux expansion ($\approx 2.5\%$), double-null balancing splits the exhaust between two targets ($\approx 1.0\%$), and a snowflake geometry flares the flux expansion further ($\approx 0.5\%$). Figure 4 and table 3 tabulate the cascade; a full-power cassette with divertor loading fraction $f_{\mathrm{div}} = 1.0$ is confirmed. The lever inventory and its ranking against alternative geometries are the subject of the companion portfolio and down-select papers [29,30].

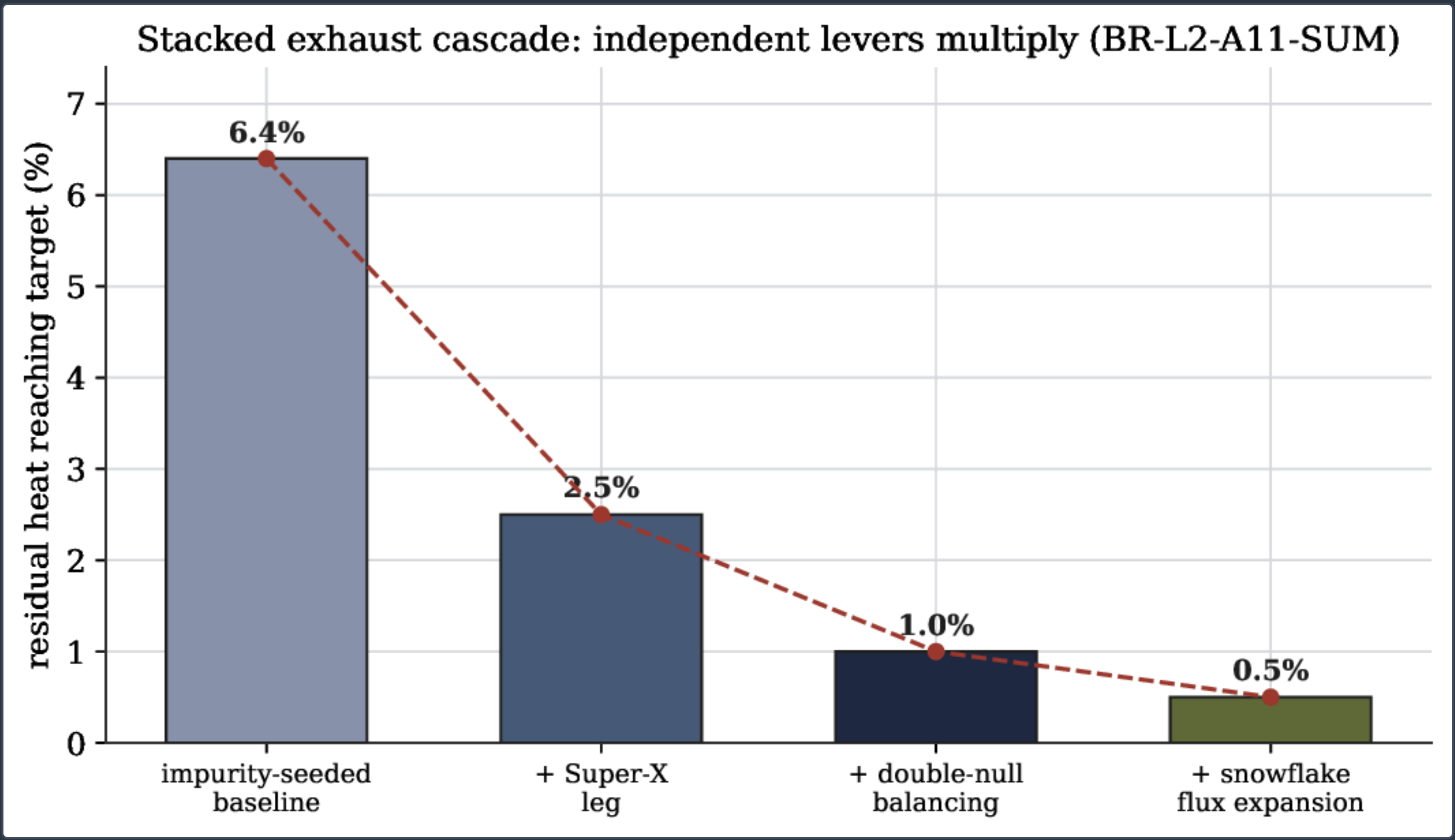

Divertor power-exhaust mitigation cascade (BR-L2-A11-SUM). Each stacked lever removes an independent fraction of the residual heat reaching the target, driving the seeded baseline of 6.4% down to $\approx 0.5\%$.

MITIGATION LEVER (CUMULATIVE)	RESIDUAL TO TARGET	TERM ACTED ON
impurity-seeded baseline	6.4%	f_{rad}, eq. (16)
+ Super-X leg	$\approx 2.5\%$	f_x, eq. (14)
+ double-null balancing	$\approx 1.0\%$	P_{SOL} split, eq. (11)
+ snowflake flux expansion	$\approx 0.5\%$	f_x, eq. (14)

Stacked exhaust levers and the residual heat fraction reaching the divertor target (BR-L2-A11-SUM).

ONE-DIMENSIONAL DETACHMENT SCAN

The detachment physics behind the seeded baseline is resolved directly. The UEDGE slab-SOL scan (BR-L2-A21) drives the target electron temperature through $14.4 \to 5.3 \to 1.05$ eV across the seeding scan (figure 5), passing through the ~ 5 eV detachment threshold and reaching the low-temperature, high-recycling regime where eq. (13) predicts pressure balance to break. The upstream-to-target density ratio reaches $n_t/n_u \approx 31$ against an analytic arbiter of ≈ 27, and the scan establishes that impurity seeding is both mandatory and sufficient to reach detachment-relevant conditions.

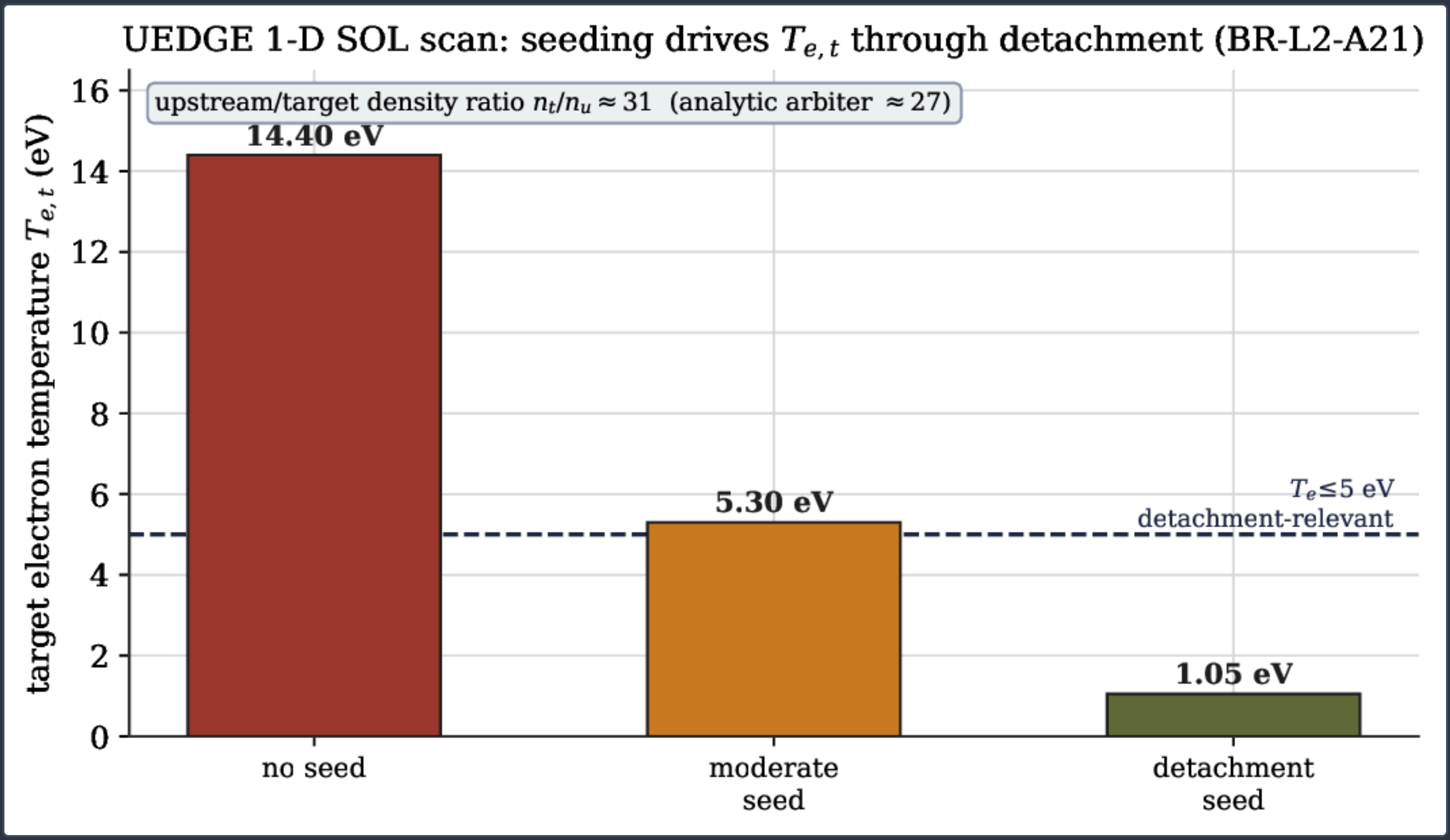

UEDGE one-dimensional SOL scan (BR-L2-A21): the target electron temperature falls through $14.4 \to 5.3 \to 1.05$ eV as the seed fraction increases, crossing the ~ 5 eV detachment threshold. The upstream/target density ratio reaches $n_t/n_u \approx 31$ (analytic arbiter ≈ 27).

WHY SUPER-X AND DETACHMENT ARE BOTH REQUIRED

Figure 6 plots the target perpendicular load of eq. (14) against the radiated fraction for the conventional and Super-X legs. The conventional leg, attached at $1370\,\mathrm{MW\,m^{-2}}$, needs $f_{\mathrm{rad}} = 99.3\%$ to fall below the $10\,\mathrm{MW\,m^{-2}}$ limit—an impractically thin margin against radiative collapse—while the Super-X leg, attached at $171\,\mathrm{MW\,m^{-2}}$ by virtue of its eightfold flux expansion, reaches the limit at $f_{\mathrm{rad}} = 94.2\%$, inside the detachment window that opens at $\sim 91\%$ (HX-14/14b). Neither geometry alone nor detachment alone is sufficient; the two together place the target load inside the engineering window, which is exactly why the cascade of §4.3 stacks the flux-expansion lever underneath the radiative one. The real-time regulation that holds the radiated fraction at the operating point without tipping into collapse is the subject of the companion detachment-control paper [32].

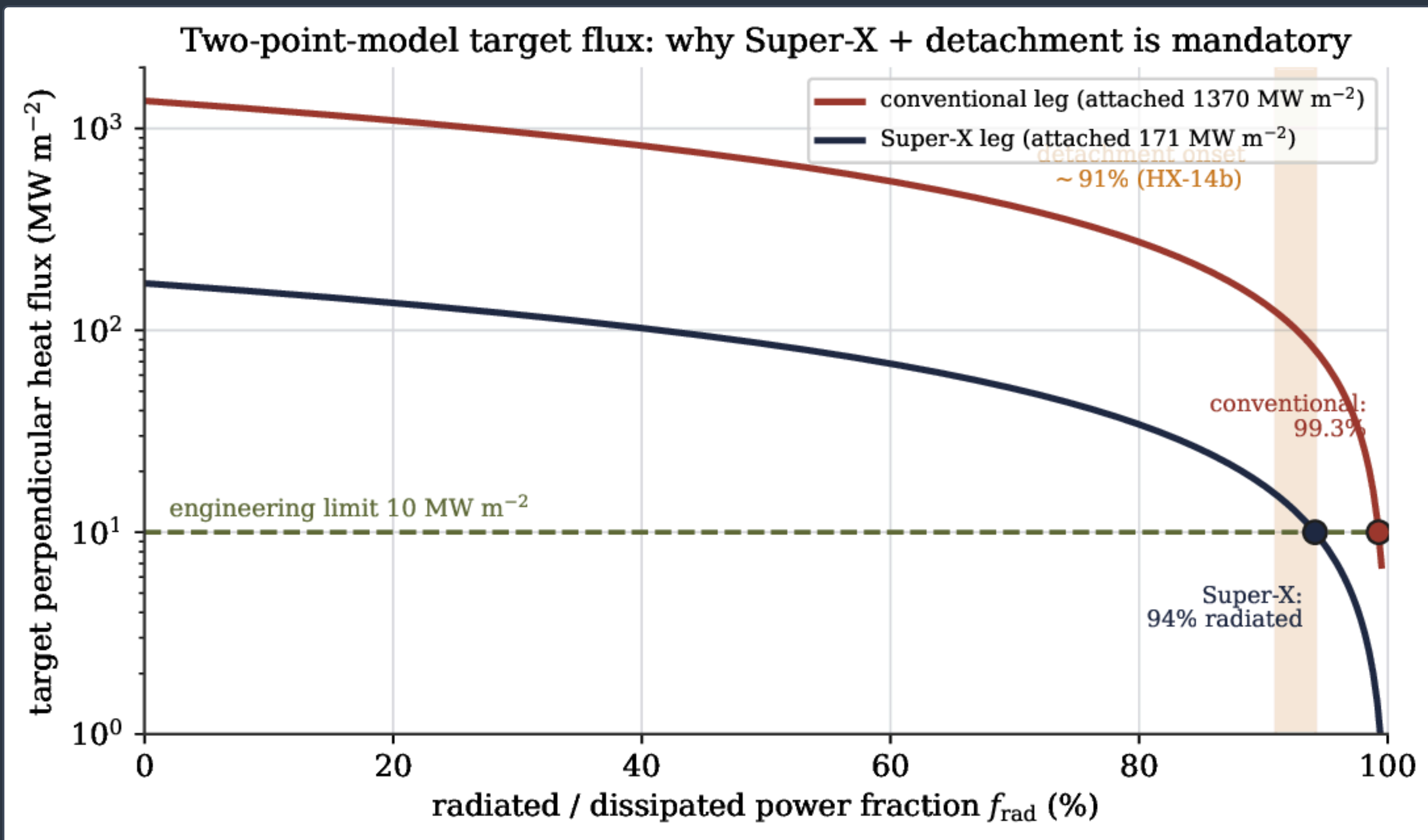

Two-point-model target load of eq. (14) versus radiated fraction (HX-14/14b). The Super-X leg (attached $171\,\mathrm{MW\,m^{-2}}$) reaches the $10\,\mathrm{MW\,m^{-2}}$ limit at $f_{\mathrm{rad}} = 94.2\%$, inside the detachment window opening near 91%; the conventional leg (attached $1370\,\mathrm{MW\,m^{-2}}$) requires an impractical 99.3%.

THE FLOWING-LITHIUM ALTERNATIVE

A second, independent exhaust path replaces the seeded gas target with a flowing-lithium vapor-box divertor, whose evaporation-limited surface can accept a fixed heat flux set by the film velocity. Figure 7 shows the handled surface heat flux rising from 2.8 to 4.9 to $6.7\,\mathrm{MW\,m^{-2}}$ as the film velocity increases through 2, 5 and $10\,\mathrm{m\,s^{-1}}$ (HX-16), comfortably above the $\lesssim 0.5\,\mathrm{MW\,m^{-2}}$ load that the detached cascade delivers to the target. The flowing-lithium option therefore provides a large surface-load margin and a co-benefit of in-loop tritium extraction; its full treatment, including the vapor-box redeposition requirement, is the companion vapor-box divertor paper [31].

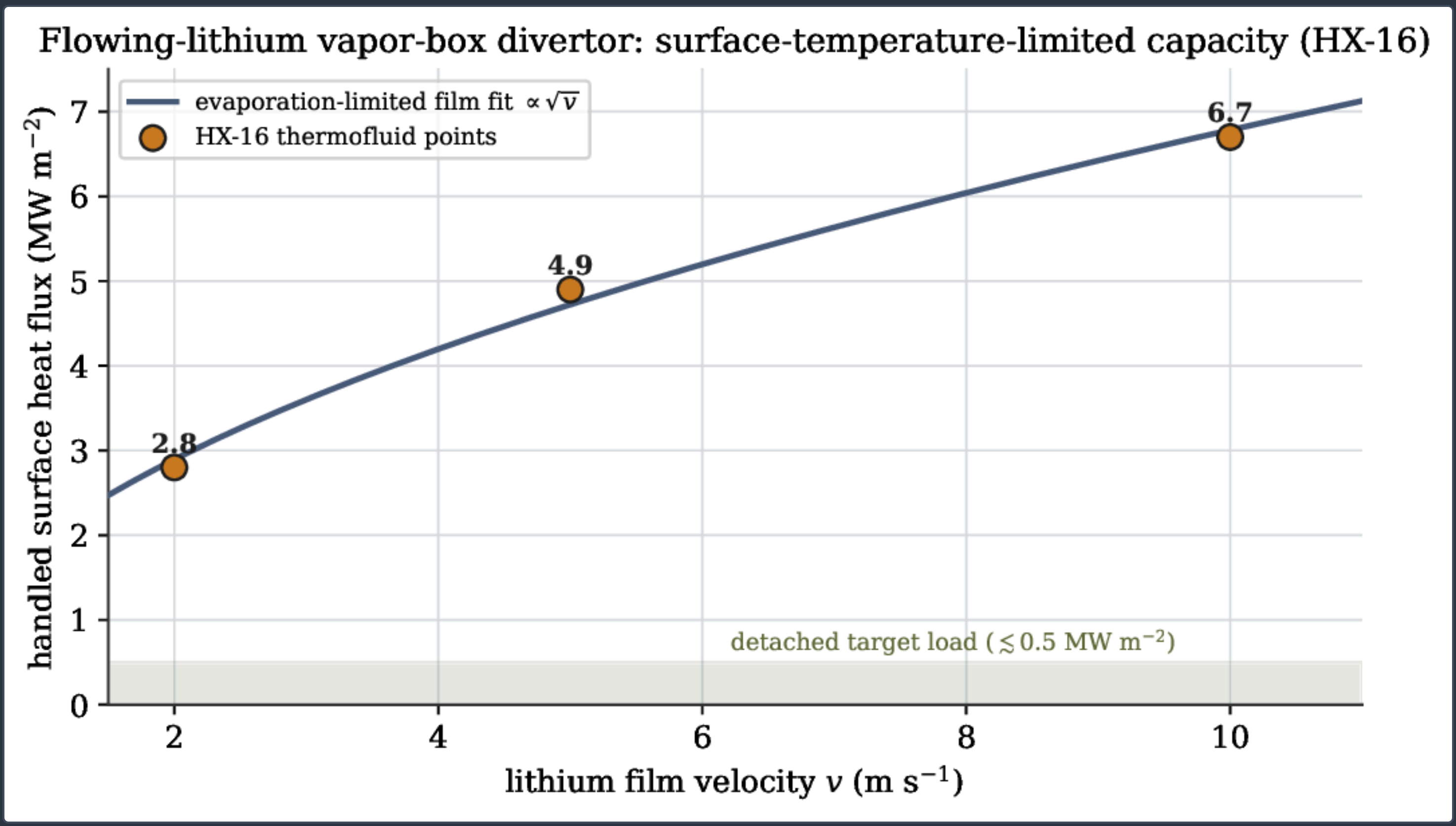

Flowing-lithium vapor-box divertor: surface-temperature-limited handled heat flux versus film velocity (HX-16). The three thermofluid points ($2.8/4.9/6.7\,\mathrm{MW\,m^{-2}}$ at $2/5/10\,\mathrm{m\,s^{-1}}$) sit far above the detached-target load band.

THE WALK-AWAY DECAY-HEAT TRANSIENT

Figure 8 shows the passive decay heat of eqs. (17)–(18). The load falls from 0.95 MW at 1 s—roughly 1% of the operating thermal power—to 95 kW at one day, following the fitted power law $P_d(t) = 0.95\,(t/1\text{ s})^{-0.203}$ MW (BR-L1-A9). Over this transient the passive-rejection balance of eq. (19) holds structural temperatures at or below 710 °C, inside the material limit, so no powered cooling is required to reach a safe state. This passive walk-away is the property that most simplifies the plant-level accident and environmental case [34].

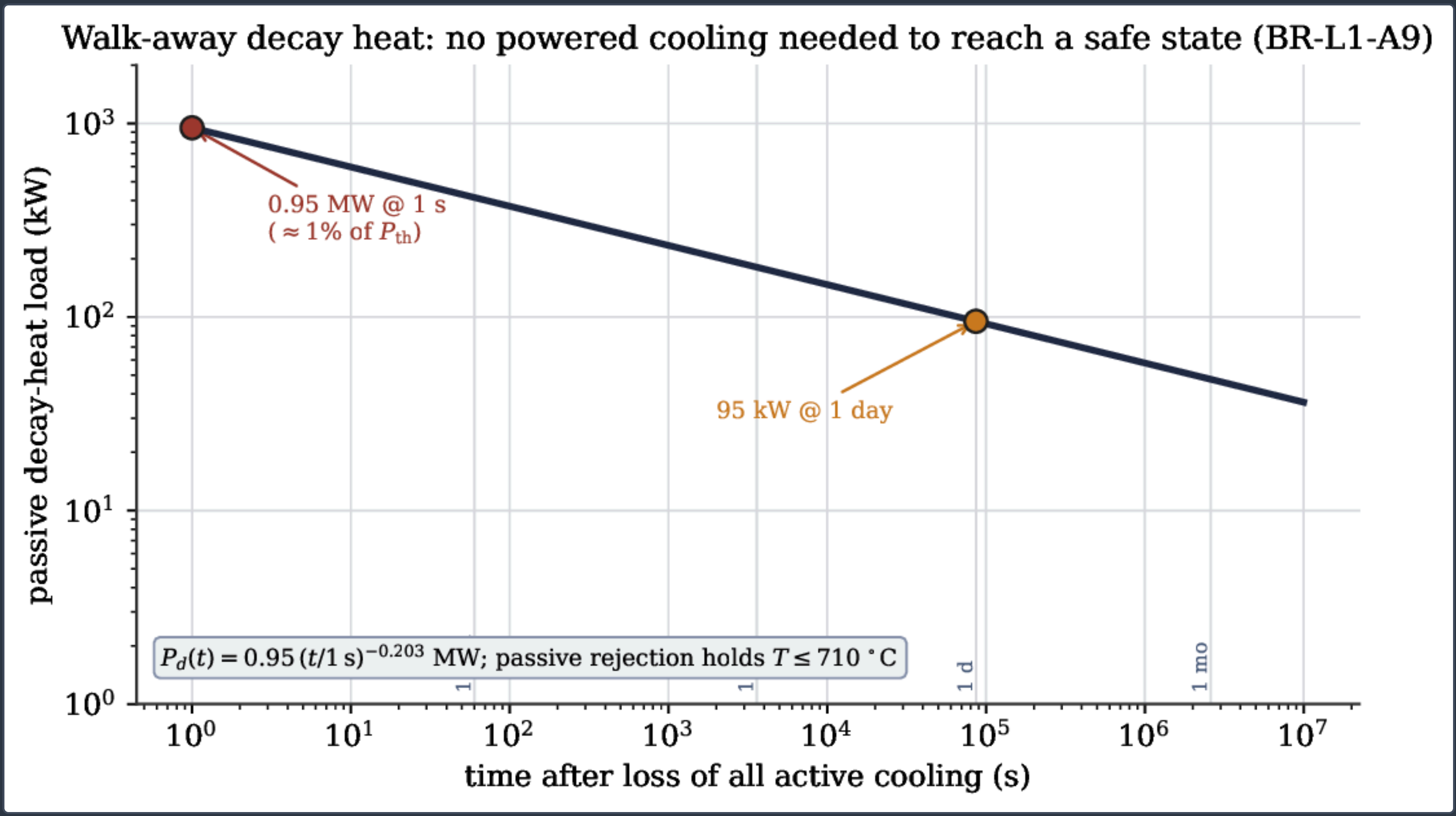

Walk-away decay heat (BR-L1-A9). The passive load falls from 0.95 MW at 1 s to 95 kW at one day along $P_d(t) = 0.95\,(t/1\text{ s})^{-0.203}$ MW (eq. 18); passive rejection holds structural temperatures at or below 710 °C.

THE PUMPING-VERSUS-TEMPERATURE-RISE TRADE

Because the coolant flow is fixed by eq. (4), the choice of temperature rise ΔT trades pumping power against coolant outlet temperature. Figure 9 plots the ΔT^{-3} scaling of eq. (8) anchored to the BV-06 operating point (200 K, 5.8 MW, 5.2% of P_{th}): halving ΔT to 100 K would raise pumping to 46 MW, while raising ΔT sharply cuts pumping at the cost of a hotter outlet and reduced first-wall margin. The exact closure of the coolant balance (§4) is what makes this a clean design trade—the energy balance is not reopened as ΔT moves.

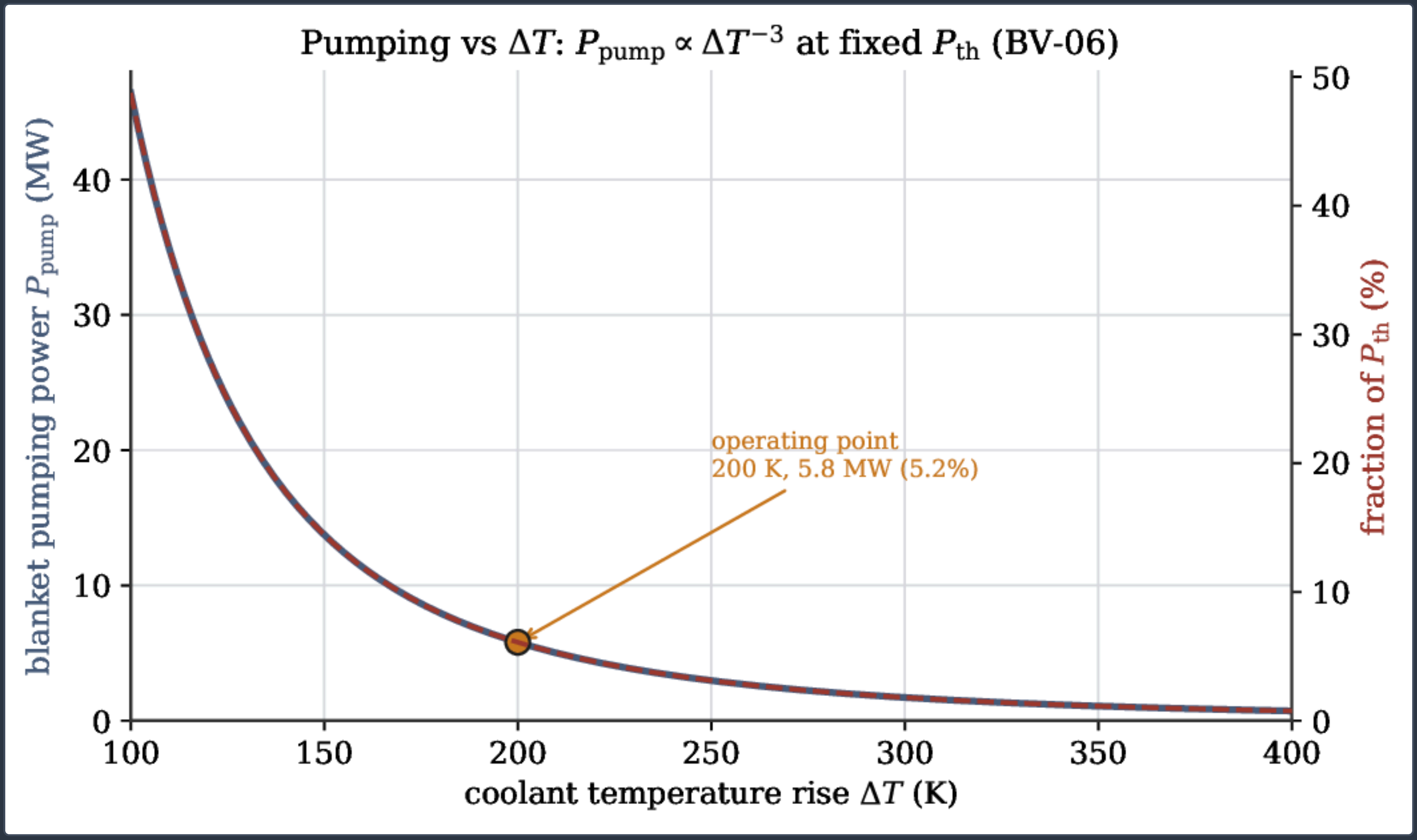

Pumping power versus coolant temperature rise, $P_{\mathrm{pump}} \propto \Delta T^{-3}$ at fixed P_{th} (eq. 8), anchored to the BV-06 operating point (200 K, 5.8 MW = 5.2% of P_{th}).

SENSITIVITY OF THE THERMAL MARGIN

Figure 10 ranks the local sensitivity of the peak-temperature margin to the governing parameters, computed from the analytic conduction, convection and two-point models of §2. The divertor radiated fraction dominates by a wide margin—a consequence of the near-unity dissipation required by eq. (14)—followed by the coolant-channel depth, the coolant temperature rise and the surface heat flux; the wall conductivity and the convective coefficient enter more weakly. The ranking identifies where design and control effort is best spent: on holding f_{rad} and on the channel-depth gate.

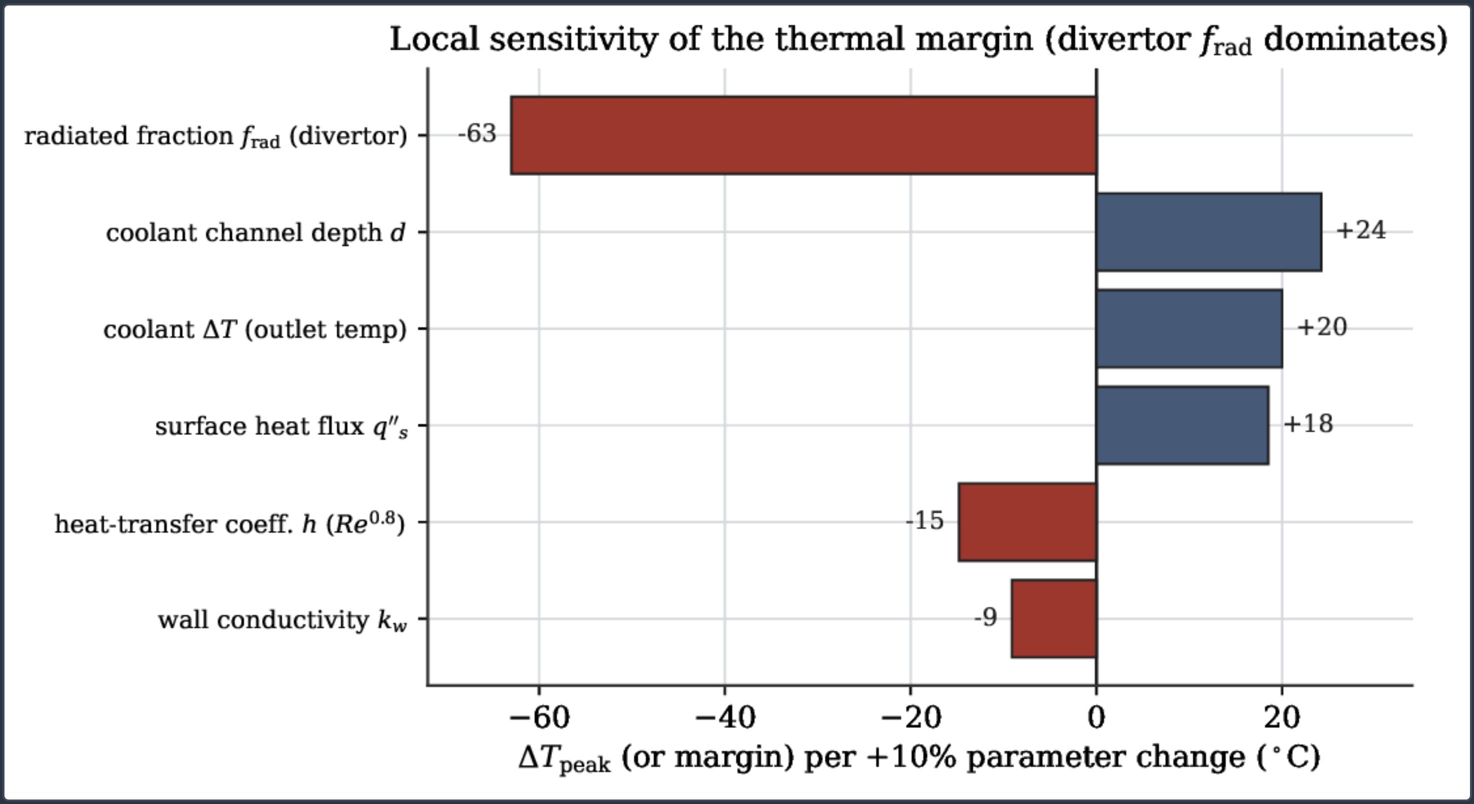

Local sensitivity of the thermal margin to the governing parameters (from the models of §2). The divertor radiated fraction f_{rad} dominates; blue bars raise the peak temperature (reduce margin), red bars lower it.

§ 5

Discussion

The thermal path closes with margin at every stage, and each result can be read against the published record. The coolant balance is not merely adequate but exact: the closure $\dot{m}c_p\Delta T = 95.2$ MW leaves the design free to trade coolant temperature against pumping power (figure 9) without reopening the energy balance, a freedom that DEMO helium-cooled blanket studies exploit at comparable multiplication $M_E \approx 1.1$–1.2 [18,19]. The first-wall peak-temperature stack sits inside the reduced-activation ferritic- martensitic envelope, and the ≤ 6 mm channel gate is the same order of near-wall cooling refinement that DEMO first-wall thermal analyses require [19]; the self-cooled-lithium variant at 516 °C is the more comfortable of the two options on temperature alone.

The exhaust result is where the compact ST is most severe and where the analysis is most quantitative. The sub- millimetre $\lambda_q = 0.21$ mm follows directly from the Eich poloidal-field scaling [5] at 9.66 MA, and the resulting $27.4\ \mathrm{GW\,m^{-2}}$ parallel flux is what forces the stacked solution. Our conclusion—that detachment is mandatory and that a flux-expanding geometry must sit underneath the radiative lever—is the same conclusion reached for the ARC pilot plant, whose long-legged high-field divertor study likewise finds advanced geometry necessary to manage the compact-high-field exhaust [15], and it is consistent with the ITER tungsten-divertor physics basis, which sets the $\sim 10\ \mathrm{MW\,m^{-2}}$ steady limit we adopt [17]. The detachment physics itself is validated in the harder, code-resolved way rather than asserted: the UEDGE scan resolves the T_t collapse through 5 eV that the two-point model of eq. (13) and the detachment literature [8,6] predict, and the SD1D/BOUT++ cross-check (HX-14b) independently finds that a sub-percent seed detaches the target at a comparable λ_q, so the two libraries agree on the physically load-bearing quantity—the seed fraction required for detachment. The flowing-lithium alternative (figure 7) follows the vapor-box concept of Goldston *et al.* [16] and gives a second, independent exhaust path with a large surface-load margin. The impurity-seeding requirement itself is exactly the DEMO-class exhaust conclusion of Kallenbach *et al.* [9].

Finally, the walk-away decay-heat transient makes the safety case passive. The $\approx 1\%$-of-P_{th} decay load at 1 s and its further order-of-magnitude fall within a day, computed by activation depletion in the FISPACT-II class [22], are small enough that the passive-rejection balance of eq. (19) bounds the structural temperature at 710 °C without operator action—the property that most simplifies licensing for a compact, near-urban machine and the input to the plant-level environmental case [34].

§ 6

Limitations

One honest gate bounds the exhaust claim. The two-dimensional SOLPS-ITER detachment solve on this equilibrium was blocked by a grid-topology issue in the Carre2 chain (BR-L2-A11b-s3), so the detachment operating point is presently anchored by the one-dimensional UEDGE scan (BR-L2-A21), the SD1D/BOUT++ cross-check (HX-14b), and the stacked-lever portfolio (BR-L2-A11-SUM) rather than by a converged two-dimensional number. Completing the two-dimensional arbiter on the same built toolchain is the confirming calculation and is in progress; it does not change the closed coolant balance or the walk-away result, both of which are independently anchored.

§ 7

Conclusion

The Hyperion breeder's heat path is closed and quantified. The helium-cooled blanket recovers $P_{\mathrm{th}} = 95.2$ MW at an energy multiplication $M_E = 1.119$, and a $91.7\ \mathrm{kg\,s^{-1}}$ coolant flow across a 200 K rise removes it exactly, $\dot{m}c_p\Delta T = 95.2$ MW; the first-wall peak temperature is held inside the material envelope by a ≤ 6 mm channel gate, with a self-cooled-lithium variant at 516 °C; the $27.4\ \mathrm{GW\,m^{-2}}$ parallel exhaust is brought below the $10\ \mathrm{MW\,m^{-2}}$ target limit by a stacked cascade reaching $\approx 0.5\%$ residual heat, with detachment resolved in one dimension and cross-checked in a second library; and the machine walks away passively, decay heat falling to 95 kW within a day while passive rejection holds structural temperatures at or below 710 °C. Produced end to end by the NVIDIA GPU HPC campaign and reproduced by independent libraries, the thermal-hydraulic design is buildable, its coolant balance is closed to the first digit, and its safety case does not rely on active cooling.

Acknowledgments tocsectionAcknowledgments Part of the Kronos Fusion Energy 2026 design series. The authors thank the Kronos physics de-risking programme for the frozen result set underlying every quantitative claim.

Reproducibility. The thermal balance, first-wall temperature stack, divertor cascade, detachment scan and decay-heat anchors are frozen results in the Kronos De-Risking Register [27] (BR-L1-A5, BR-L1-A9, BV-06, BR-SX-15, HX-14/14b, BR-L2-A21, BR-L2-A11-SUM, BR-L2-A11b-s3), regenerable from the archived blanket, thermofluid and edge-transport decks and from the figure-generation script deposited with this paper. This paper is archived at its DOI doi:10.5281/zenodo.22645836; official version: https://www.kronosfusionenergy.com/publications/blanket-and-divertor-thermal-hydraulics-for-a-compact-s.html and its official page https://www.kronosfusionenergy.com/publications/blanket-and-divertor-thermal-hydraulics-for-a-compact-s.html; the register is archived at doi:10.5281/zenodo.22133057.

Data availability tocsectionData availability The power-balance, temperature-stack, cascade, detachment-scan, flowing-lithium, decay-heat, pumping-trade and sensitivity data used for figures 2–10 are archived with the deposit at doi:10.5281/zenodo.22645836 and trace to the register [27] by the serial identifiers cited inline. Any economic analysis is reported separately and is not part of the public deposit.

Competing interests tocsectionCompeting interests Provisional patent applications relating to aspects of this work have been filed.

tocsectionReferences

APPARATUS

Portfolio, People & Record

The intellectual-property estate, the people who built it, the limitations that gate it, and the sources it rests on.

1	4	40	27
GRANTED PATENT	2026 PROVISIONALS	TEAM MEMBERS	2022 PROVISIONALS

INTELLECTUAL PROPERTY

The patent portfolio

The estate spans a granted high-field magnet patent, pending utility and 2026 provisional filings that map to the two products, a digital-twin control provisional, a registered trademark application, and the original 2022 provisional family. Every patentable disclosure in the five-paper arXiv drop was protected **before** publication: the breeder and burner provisionals were filed 1–2 August, and a publication-gap omnibus filing the evening before the drop swept up the DEC, plasma-control, and REBCO-winding matter of the three otherwise-unprotected papers. Patent numbers and application serials are matters of public record; claim scope is summarised, not reproduced.

GRANTED & PENDING UTILITY

US 12,009,112	High-field tilted graded-REBCO magnet architecture (KRONO-002A) *· app. 17/878,550*	GRANTED
US 17/878,507	Core device / method (KRONO-001A) *· utility*	PENDING

2026 PROVISIONAL FILINGS — MAPPED TO THE PRODUCTS

64/124,209	Hyperion — spherical-tokamak tritium / helium-3 foundry *· breeder · filed Aug 2026*	FILED
64/124,220	Aegis / MetroVolt — synchrotron-cutoff, fuel-selection & plug-winding *· generator · filed Aug 2026*	FILED
64/115,167	KRONOS-CTRL digital-twin plant control *· provisional · filed Jul 2026*	FILED
64/005,440	Integrated spherical-tokamak fusion architecture *· early integrated-architecture filing · filed Mar 2026*	FILED
64/105,530	Negative-triangularity spherical-tokamak architecture *· foundational ST filing · filed Jul 2026*	FILED
64/128,097	Publication-gap omnibus — quasineutral two-species expander DEC · provenance-gated / latency-split plasma control · as-built high-field winding & conductor architecture *· filed 7 Aug 2026, the evening before the arXiv drop*	FILED

TRADEMARK & ORIGIN

FTK-98801894	Kronos Fusion Energy — trademark application	FILED
KR-2022-*	Original provisional family (KR-2022-00001 … 00027) *· 27 filings, 2022*	PRIORITY

The narrow, defensible magnet novelty — the specific conductor and the digital-twin winding optimisation, not high-field REBCO as a category — is the commercial core that can earn ahead of any Q > 1 milestone, with markets in fusion magnet supply, MRI/NMR, accelerators, and proton therapy. The claim is scoped honestly: the high field is a *system field* result, not a stand-alone-coil record; the small-bore plug coil is structurally infeasible as a bare winding but resolved by a stress-managed structural shield (feasible-pending-FEA); and the winding-tape experiment returned a *null result*. The value is the method, not a field record.

THE TEAM

Founding partners, board, advisors & auditors

Kronos is built by a bench of advanced-fuel-fusion, high-field-magnet, direct-conversion, and materials specialists, with a board and operations team drawn from defense, national laboratories, and industry. Dates are shown as ranges; where a tenure has ended or is term-ending, the range says so.

FOUNDING PARTNERS — SCIENCE

Dr. Gerald Kulcinski
Co-Founder · Helium-3 & Advanced-Fuel Fusion
UW–Madison · 2023–Present

Dr. Carl Weggel
Chief Scientist / S.M.A.R.T. Design
MIT Alcator Program · 2022–Present

Dr. Robert J. Weggel
Magnetic Field Design
MIT Magnet Lab · 2022–Present

BOARD

Priyanca Ford
Founder & CEO · Executive Board
2022–Present

Bandel Carano
Finance / Strategy
Oak Investment Partners / Stanford · 2025–2026

Patrick Schweiger
Fusion Device Engineering
Oklo / CFS / TerraPower · 2025–Present

SCIENTIFIC ADVISORS

Dr. Steven O. Dean
Fusion Policy & History
DOE / Fusion Power Associates · 2025–Present

Dr. Patrick H. Diamond
Plasma Turbulence & Transport
UC San Diego · 2025–Present

Dr. Jack J. Dongarra
HPC & Numerical Algorithms
Turing Award · 2025–Present

Dr. Nasr M. Ghoniem
Chief Material Scientist
UCLA · 2025–Present

Dr. Siegfried Glenzer
Plasma Physics & Laser Fusion
Stanford / SLAC · 2022–Present

Dr. David A. Hammer
Pulsed-Power Fusion
Cornell · 2025–Present

Dr. Donald A. Spong
Plasma Theory & Confinement
ORNL · 2025–Present

Dr. Curtis Smith
Risk Assessment & Nuclear PRA
MIT / Idaho National Lab · 2025–Present

RADM (Ret.) David Goggins
Naval Engineering & Power-Plant Design
U.S. Navy · 2023–2026

Dr. Konstantin Batygin
Mathematician
Caltech · 2022–2025

Dr. Ruben Fair
Magnet Design / ITER Liaison
PPPL / Jefferson Lab · 2022–2025

Dr. Paul S. Weiss
Materials & Nanotechnology
UCLA · 2022–2025

SCIENTIFIC AUDITORS

Dr. Wilfred A. Cooper
Plasma Equilibrium Theory
EPFL / Swiss Plasma Center · 2025–Present

Dr. Ahmed Hassanein
Plasma–Material Interactions
Purdue / Argonne · 2025–Present

Dr. Patrick E. Hopkins
Extreme Thermal Materials
U. of Virginia · 2025–Present

Dr. Peter Hosemann
Materials Joining & Structural Integrity
UC Berkeley · 2025–Present

Dr. Travis W. Knight
Advanced Nuclear Fuels & Systems
U. of South Carolina · 2025–Present

Dr. Philippe Lebrun
Cryogenics & Magnet Cooling
CERN · 2025–Present

Dr. Nitendra Singh
Nuclear Safety & Fuel Cycle
ITER · 2025–Present

Dr. Guido Van Oost
Magnetic Confinement & Fusion Systems
Ghent University · 2025–Present

Dr. Gary S. Was
Radiation Materials & Structural Integrity
U. of Michigan · 2025–Present

Dr. Ray Sedwick
Direct Energy Conversion
U. of Maryland · 2025

OPERATIONS

Michael Laughlin
Chief Operating Officer
2022–Present

Martin Owens
Chief Strategy Officer
LANL / GE Hitachi · 2022–Present

MG (Ret.) Paul Pardew
Chief Contracting Officer
Army Contracting Command · 2022–Present

David Beck
Fusion Commercialization
U.S. Space Force · 2024–Present

Sushma Bhatia
Environmental & Legislative
Google · 2022–Present

Michael De Frenza
Technology Licensing
2023–Present

MG (Ret.) Robin L. Fontes
Cybersecurity & Defense
Army Cyber Command · 2022–Present

Vijay Gehani
Supply Chain & Components
INOX India · 2024–Present

Jon Michel Greenwood
IT & AI Infrastructure
Live Nation · 2023–Present

Brian C. O'Neill
National Security
CIA / ODNI · 2022–Present

Gen. (Ret.) Gustave F. Perna
DoD Liaison
Operation Warp Speed · 2022–2023

Andrea Romero
Marketing Lead
2022–Present

Legal counsel is retained; those roles are held on the internal roster and are not listed here.

SOURCES

References

1 J E Menard *et al*, Fusion nuclear science facilities and pilot plants based on the spherical tokamak, *Nucl. Fusion* **56** 106023 (2016). doi:10.1088/0029-5515/56/10/106023

2 B N Sorbom *et al*, ARC: a compact, high-field, fusion nuclear science facility and demonstration power plant with demountable magnets, *Fusion Eng. Des.* **100** 378 (2015). doi:10.1016/j.fusengdes.2015.07.008

3 M E Austin *et al*, Achievement of reactor-relevant performance in negative triangularity shape in the DIII-D tokamak, *Phys. Rev. Lett.* **122** 115001 (2019). doi:10.1103/PhysRevLett.122.115001

4 A Marinoni, O Sauter and S Coda, A brief history of negative triangularity tokamak plasmas, *Rev. Mod. Plasma Phys.* **5** 6 (2021). doi:10.1007/s41614-021-00054-0

5 T Eich *et al*, Scaling of the tokamak near the scrape-off layer H-mode power width and implications for ITER, *Nucl. Fusion* **53** 093031 (2013). doi:10.1088/0029-5515/53/9/093031

6 A Loarte *et al*, Chapter 4: Power and particle control (Progress in the ITER Physics Basis), *Nucl. Fusion* **47** S203 (2007). doi:10.1088/0029-5515/47/6/S04

7 P C Stangeby, *The Plasma Boundary of Magnetic Fusion Devices*, IOP Publishing, Bristol (2000).

8 S I Krasheninnikov, A S Kukushkin and A A Pshenov, Divertor plasma detachment, *Phys. Plasmas* **23** 055602 (2016). doi:10.1063/1.4948273

9 A Kallenbach *et al*, Impurity seeding for tokamak power exhaust: from present devices via ITER to DEMO, *Plasma Phys. Control. Fusion* **55** 124041 (2013). doi:10.1088/0741-3335/55/12/124041

10 S Wiesen *et al*, The new SOLPS-ITER code package, *J. Nucl. Mater.* **463** 480 (2015). doi:10.1016/j.jnucmat.2014.10.012

11 X Bonnin *et al*, Presentation of the new SOLPS-ITER code package for tokamak plasma edge modelling, *Plasma Fusion Res.* **11** 1403102 (2016). doi:10.1585/pfr.11.1403102

12 D Reiter, M Baelmans and P B\"orner, The EIRENE and B2-EIRENE codes, *Fusion Sci. Technol.* **47** 172 (2005). doi:10.13182/FST47-172

13 T D Rognlien, J L Milovich, M E Rensink and G D Porter, A fully implicit, time dependent 2-D fluid code for modeling tokamak edge plasmas, *J. Nucl. Mater.* **196–198** 347 (1992). doi:10.1016/S0022-3115(06)80058-9

14 B D Dudson, M V Umansky, X Q Xu, P B Snyder and H R Wilson, BOUT++: a framework for parallel plasma fluid simulations, *Comput. Phys. Commun.* **180** 1467 (2009). doi:10.1016/j.cpc.2009.03.008

15 A Q Kuang *et al*, Conceptual design study for heat exhaust management in the ARC fusion pilot plant, *Fusion Eng. Des.* **137** 221 (2018). doi:10.1016/j.fusengdes.2018.09.007

16 R J Goldston, R Myers and J Schwartz, The lithium vapor box divertor, *Phys. Scr.* **T167** 014017 (2016). doi:10.1088/0031-8949/T167/1/014017

17 R A Pitts *et al*, Physics basis for the first ITER tungsten divertor, *Nucl. Mater. Energy* **20** 100696 (2019). doi:10.1016/j.nme.2019.100696

18 G Federici *et al*, An overview of the EU breeding blanket design strategy as an integral part of the DEMO design effort, *Fusion Eng. Des.* **141** 30 (2019). doi:10.1016/j.fusengdes.2019.01.141

19 M Abdou *et al*, Blanket/first wall challenges and required R&D on the pathway to DEMO, *Fusion Eng. Des.* **100** 2 (2015). doi:10.1016/j.fusengdes.2015.07.021

20 P K Romano, N E Horelik, B R Herman, A G Nelson, B Forget and K Smith, OpenMC: a state-of-the-art Monte Carlo code for research and development, *Ann. Nucl. Energy* **82** 90 (2015). doi:10.1016/j.anucene.2014.07.048

21 D A Brown *et al*, ENDF/B-VIII.0: the 8th major release of the nuclear reaction data library, *Nucl. Data Sheets* **148** 1 (2018). doi:10.1016/j.nds.2018.02.001

22 J-Ch Sublet, J W Eastwood, J G Morgan, M R Gilbert, M Fleming and W Arter, FISPACT-II: an advanced simulation system for activation, transmutation and material modelling, *Nucl. Data Sheets* **139** 77 (2017). doi:10.1016/j.nds.2017.01.002

23 H G Weller, G Tabor, H Jasak and C Fureby, A tensorial approach to computational continuum mechanics using object-oriented techniques, *Comput. Phys.* **12** 620 (1998). doi:10.1063/1.168744

24 A J Creely *et al*, Overview of the SPARC tokamak, *J. Plasma Phys.* **86** 865860502 (2020). doi:10.1017/S0022377820001257

25 F P Incropera, D P DeWitt, T L Bergman and A S Lavine, *Fundamentals of Heat and Mass Transfer*, 7th edn., Wiley, New York (2011).

26 J Wesson, *Tokamaks*, 4th edn., Oxford University Press, Oxford (2011).

27 P I Ford, *Kronos Physics De-Risking Register* (v8), Kronos Fusion Energy 2026 series. doi:10.5281/zenodo.22133057

28 P I Ford, CAD-faithful neutronics for a compact spherical-tokamak breeder: STEP-to-DAGMC Monte-Carlo transport reproducing the 3-D net tritium-breeding ratio, Kronos Fusion Energy 2026 series. doi:10.5281/zenodo.22645881; https://www.kronosfusionenergy.com/publications/cad-faithful-neutronics-for-a-compact-spherical-tokamak.html

29 P I Ford and G L Kulcinski, A stacked detachment portfolio for a compact spherical-tokamak breeder: Super-X, double-null and snowflake geometries that cut the required argon seed fraction, Kronos Fusion Energy 2026 series. doi:10.5281/zenodo.22645742; https://www.kronosfusionenergy.com/publications/divertor-portfolio.html

30 P I Ford and G L Kulcinski, A divertor-exhaust concept down-select for a compact spherical-tokamak breeder, Kronos Fusion Energy 2026 series. doi:10.5281/zenodo.22645933; https://www.kronosfusionenergy.com/publications/a-divertor-exhaust-concept-down-select-for-a-compact-sp.html

31 P I Ford and G L Kulcinski, A flowing-lithium vapor-box divertor with molten-salt in-loop tritium extraction for a compact spherical-tokamak breeder, Kronos Fusion Energy 2026 series. doi:10.5281/zenodo.22645750; https://www.kronosfusionenergy.com/publications/flowing-lithium-vapor-box-divertor.html

32 P I Ford and G L Kulcinski, Real-time detachment control for a Super-X divertor in a compact spherical-tokamak breeder, Kronos Fusion Energy 2026 series. doi:10.5281/zenodo.22645874; https://www.kronosfusionenergy.com/publications/real-time-detachment-control-for-a-super-x-divertor-in-.html

33 P I Ford and G L Kulcinski, First-wall thermomechanics and fatigue life of plasma-facing components under combined surface and volumetric loading in a compact spherical-tokamak breeder, Kronos Fusion Energy 2026 series. doi:10.5281/zenodo.22645850; https://www.kronosfusionenergy.com/publications/first-wall-thermomechanics-and-fatigue-life-of-plasma-f.html

34 P I Ford and G L Kulcinski, Environmental profile, accident analysis and the tritium safety case for a multi-kilogram breeder plant, Kronos Fusion Energy 2026 series. doi:10.5281/zenodo.22645754; https://www.kronosfusionenergy.com/publications/inherent-safety-and-environmental-case.html

COLOPHON

How this document was made

The Kronos Fleet — Combined Editorial, 2026 is set in **Fraunces** (display), **Gelasio** (text), and **IBM Plex Mono** (data & equations), carried forward from the Kronos editorial design system.

The figures are rendered at 300 dpi from the deposited generator scripts; the document is composed as a single self-contained file with embedded fonts and imagery, paginated to US Letter, and rendered to PDF through a headless Chromium engine in matched light and dark editions.

Every headline quantity carries an evidence class; withdrawn and restated values are marked as such. Nothing herein is frozen beyond the founder-approved Tier-A set.

Explore it live — turn the interactive 3-D model, run the deposited solvers in the physics validator, and watch the companion film series.

LEGAL NOTICE

Notice, status, and distribution

Conceptual design & simulation study. This document reports a conceptual design and simulation study. It is not a construction commitment, a safety-analysis report, a regulatory filing, or an offer of securities. Forward-looking statements — schedules, costs, market sizes, and performance — are estimates subject to the limitations set out in the Simulations part and may change.

Numbers and their classes. Quantities are reported with evidence classes and case labels; modelled, assumed, and requirement-class values are identified as such and are not to be quoted without their labels.

Public edition. This edition carries the physics and design only; all financial, funding, and defense-commercial content has been removed for public distribution. The scientific text corresponds to the arXiv and journal submissions.

THE 2026 KRONOS SERIES

One programme, many papers

This editorial is one paper in the Kronos 2026 series — a real fusion company's complete, reproducible physics record for a spherical-tokamak breeder and its low-neutron D–^{3}He tandem-mirror burners. Every headline number is a frozen anchor in the Physics De-Risking Register.

Explore the whole programme: the De-Risking Register, the interactive 3-D model, and the physics validator.

KRONOS FUSION ENERGY

Blanket and Divertor Thermal-Hydraulics for a Compact Spherical-Tokamak Breeder: Coolant Heat Removal, Peak-Temperature Margins, and the Walk-Away Safety Case

A real fusion company building real machines. Explore the science, live.

Zenodo · doi:10.5281/zenodo.22645836

Read on kronosfusionenergy.com

The Physics De-Risking Register